PAPER

Check for updates

Towards smart free form-factor 3D printable batteries

Heftsi Ragones,†[a] Svetlana Menkin, †[a] Yosi Kamir,[a] Alex Gladkikh,[b] Tzach Mukra,[a] Gabor Kosa[c] and Diana Golodnitsky *[ab]

Continuous novelty as the basis for creative advance in rapidly developing different form-factor microelectronic devices requires seamless integrability of batteries. Thus, in the past decade, along with developments in battery materials, the focus has been shifting more and more towards innovative fabrication processes, unconventional configurations, and designs with multi-functional components. We present here, for the first time, a novel concept and feasibility study of a 3D-microbattery printed by fused-filament fabrication (FFF). The reversible electrochemical cycling of 3D printed lithium iron phosphate (LFP) and lithium titanate (LTO) composite polymer electrodes *vs.* the lithium metal anode has been demonstrated in cells containing conventional non-aqueous and ionic-liquid electrolytes. We believe that by using comprehensively structured interlaced electrode networks it would be possible not only to fabricate free form-factor batteries but also to alleviate the continuous volume changes occurring during charge and discharge.

Introduction

The demand for free form-factor energy-storage devices has been recently added to the ever-growing need for high-specific-energy and high-power capability, long-cycle-life and safe energy-storage devices. Free form-factor design of energy-storage devices makes possible new implementations, never before supported by traditional battery structures. In order to enable free form-factor energy-storage devices, many efforts have been made towards the development of three-dimensional microbatteries.[1–10] The power output of a three-dimensional microbattery is expected to be up to two orders of magnitude higher than that of a two-dimensional battery of equal size, as a result of the higher ratio of electrode-surface-area to volume and lower ohmic losses. Within a battery electrode, the 3D architecture provides mesoporosity, increasing power by reducing the length of the diffusion path; in the separator region it can form the basis of a robust but porous solid, isolating electrodes and immobilizing an otherwise fluid electrolyte. Some proposed 3D architectures include the use of vertical "posts" connected to a substrate, in which a layered battery structure is formed around the posts. Other architectures are based on the deposition of electrodes and electrolyte layers on graphite mesh current collectors for anodes and cathodes or on perforated silicon, glass or polymer substrates.[1,11]

Additive manufacturing (AM), also known as 3D printing, refers to an industrial production technique that builds 3D objects by adding layer-upon-layer of material directly from computer-aided-design (CAD) files.[12] In recent years, the 3D printing technique has received increasing attention due to its viability in various applications. This method is a novel class of freeform fabrication technologies that have a variety of possibilities for the rapid creation of complex architectures at lower cost than conventional methods.[13,14] 3D printing enables the controlled creation of functional materials with three-dimensional architectures, representing a promising approach for the fabrication of next-generation electrochemical energy-storage devices and has many unique advantages over conventional manufacturing methods. It facilitates the freeform production of electrodes and other components in customized design, chemical composition, shape and porosity. In addition, it enables the microfabrication of asymmetric electrode structures, as well as the encapsulation of microbatteries. 3D printing can provide the co-fabrication or direct integration of microbatteries and external electronics, thereby enabling single-step assembly and packaging of the battery and the device. Moreover, sequential 3D printing of battery electrodes and the solid electrolyte layer meets the need for intimate contact between the electrodes and electrolytes. Despite extensive efforts in this field, the performance of current 3D-printed batteries is still far from those of state-of-the-art commercial batteries, in which the electrodes are fabricated by a conventional doctor-blade casting technique. The development of all-

[a]School of Chemistry, Faculty of Exact Sciences, Tel Aviv University, Tel Aviv, 6997801, Israel. E-mail: golod@post.tau.ac.il

[b]Applied Materials Research Center, Tel Aviv University, Tel Aviv, 6997801, Israel

[c]Intelligent Micro/Nano Systems Group, University Hospital of Basel, Bernoullistrasse 20, 4056 Basel, Switzerland

† Equal contribution.

3D-printed electrochemical devices is hindered by several technical issues such as nozzle clogging, particle aggregation in printing media, insufficient printer resolution, high electrode thickness and rough surface finish of printed parts.[3] The structure of a 3D-printed battery (3DPB) is more complex than that of conventional planar-electrode batteries, since it implies a high-aspect ratio and complex-shaped electrode architectures.[15] Printed batteries are classified into two main categories as sandwich-type and in-plane-type designs. The sandwich-type configuration, in which every component is placed in a different plane and stacked layer-by-layer, is a classic design for these electrochemical devices. Two symmetrical or asymmetrical electrode layers are separated by the electrolyte/separator layer, forming a complete battery. However, such a cell design might be limiting when there is a demand for small-footprint energy storage in the device.[12] A variation of sandwich-type configuration is the in-plane type design in which parallel microelectrodes are arranged or patterned on the same plane on a substrate. The accurately controlled distance between the electrodes can be achieved with the use of advanced microfabrication methods. In-plane batteries with integrated microelectrodes possess multiple advantages over the electrodes of 3D microbatteries prepared by deposition techniques. 3D printing offers an ideal way to achieve desirable in-plane cell architectures. In an in-plane battery system, the cathode and the anode are patterned in a very limited footprint area. Thus, complex manufacturing technologies are commonly applied to achieve this goal. Generally, a patterned mask and a resist are essential for the microelectromechanical system-based device fabrication, which leads to high cost. By contrast, 3D printing provides an alternative way to enable the direct writing and mask-free fabrication of tiny electrochemical devices with well-designed arrangements of microelectrodes.[12]

Electrodes in most of the printed batteries are prepared by extrusion-based methods. Extrusion-based 3D printing employs a three-axis motion stage to draw patterns by robotically squeezing "ink" through a micro-nozzle. This technique can be divided into droplet-based approaches (e.g., ink-jet printing and hot-melt printing) and filamentary-based approaches (e.g., robocasting and fused deposition), based on the rheological properties of ink materials.[16] Two important criteria must be addressed to formulate printable inks. First, viscoelastic properties need to be controllable so that they can flow through printing nozzles in extrusion or vibration deposition. Second, the mechanical stiffness and strength of inks must be sufficient to support the entire structure during ink-deposition and rapid-solidification processes. The use of nanomaterials is one of the most effective optimization strategies for 3D-printing processes. It is widely acknowledged that nanomaterials are advantageous for electrochemical energy storage because of their high surface area and ease of ionic transport. The combination of nanomaterials with 3D printing can be applied in two ways: (1) manually or automatically introducing nanomaterials during intermittent stoppages of 3D printing of host matrix materials, and (2) premixing the nanomaterials with host matrices, followed by 3D printing of the nanocomposite mixture. In addition, incorporating nanomaterials could greatly enhance the

mechanical properties, electrical conductivity and functionality of the host matrix materials. Furthermore, when the 3D-printed electrodes are composed of nanomaterials, the number of electrochemically active sites significantly increases.[12] Malone et al.[17] demonstrated the concept of sandwich-type all-printed batteries, based on zinc–air chemistry, by the deposition of zinc, electrolyte and catalysts, with separator media and electrodes via syringe-assisted extrusion of the active-material paste. Later, Kohlmeyer and co-workers[18] reported a series of studies on the effects of each component in optimizing the overall performance of free-standing and current-collector-embedded 3D printed LFP, LTO and LCO batteries. A PVDF-HFP separator is printed directly on top of an LFP electrode to form the all-printed battery. As a result, the printed LTO, LFP and LCO electrodes showed full utilization of their theoretical capacities and good stability with consistent performance over 100 cycles.[8] Sun and co-workers[19] conducted a pioneering work in this field in 2013 and achieved in-plane interdigitated Li-ion microbattery architectures through 3D printing on a sub-millimeter scale. LFP and LTO served as the cathode and the anode, respectively, in the Li-ion microbattery architecture. The discharge properties of LFP- and LTO-based half-cells indicated good agreement with their respective theoretical values. Fu et al.[20] have recently developed an all-component 3D lithium-ion battery with interdigitated electrodes and a solid membrane, in which graphene oxide (GO)-based composites are used as an ink to print electrodes by DIW (direct ink writing). The inks developed are aqueous GO-based electrode slurries, consisting of highly concentrated GO with cathode or anode active materials. The highly concentrated GO dispersions are extruded directly from a nozzle and deposited layer-by-layer to form electrodes. As a result of the shear stress introduced by the nozzle, the GO flakes are aligned along the extruding direction, a fact that enhances the electrical conductivity of the electrode.[20] The membrane-ink composite consisting of PVDF-co-HFP and Al_2O_3 nanoparticles is printed into the channels between the electrodes. After drying the sample, the liquid electrolyte is injected into the channel to fully soak the electrodes. The 3D-printed $LiFePO_4/Li_4Ti_5O_{12}$ full cell features a high electrode mass loading of about 18 mg cm^{-2} when normalized to the overall area of the battery. The full cell delivers initial charge and discharge capacities of 117 and 91 mA h g^{-1} with good cycling stability. Hu et al.[21,22] reported 3D printing, by slurry extrusion from an air-powered dispenser, of a novel synthesized cathode comprising $LiMn_{0.21}Fe_{0.79}PO_4$-C (LMFP) nanocrystals. Sun et al.[19] reported 3D printing of an interdigitated Li-ion microbattery consisting of $Li_4Ti_5O_{12}$ (40 nm size particles) and $LiFePO_4$ (<200 nm size particles). Highly concentrated $Li_4Ti_5O_{12}$ (57 wt% solids) and $LiFePO_4$ (60 wt% solids) inks were prepared by dispersing the particles in ethylene glycol (EG)–water solution. These suspensions were then ball-milled and this was followed by a two-step centrifugation process. The collected nanoparticles were re-dispersed by the addition of appropriate amounts of glycerol, aqueous hydroxypropyl cellulose (HPC) solution and aqueous hydroxyethyl cellulose (HEC) solution. Before printing, interdigitated gold current-collectors were patterned on a glass substrate by

a combination of lithographic patterning and e-beam deposition. After printing, the structures were annealed at 600 °C in argon gas. A thin-walled poly(methyl methacrylate) (PMMA) preform was laser-cut, placed around the microbattery, sealed with PDMS gel and cured at 150 °C. The assembly was filled with liquid electrolyte and sealed with a small glass cover with the use of additional PDMS. Zhang *et al.* used a modified two-step *in situ* method to print highly conductive graphene, where the enhanced interlayer bonding is particularly addressed.[23] Thermally reduced graphene was wrapped and covered by polylactic acid in the FDM processes. It was claimed that the strong interface bonding force could contribute to improving the conductivity of the composite and the mechanical properties in both the axial and transverse directions. Li *et al.*[24] demonstrated an extrusion-based additive manufacturing method for fabricating a hybrid 3D structure by using the conventional solution, which resolves the typical challenges in preparing solutions for the extrusion process. The results indicate that significantly enhanced areal energy and power densities can be achieved with the hybrid 3D structure. The $LiMn_2O_4$ battery prepared in such a structure shows superior performance (117.0 mA h g^{-1} and 4.5 mA h cm^{-2}), in terms of specific capacity and areal capacity. In recent years, an extrusion-based process named fused-deposition modelling (FDM) or fused-filament fabrication (FFF) has emerged as the most widely used 3D printing process. In this technique, thermoplastic materials are heated and extruded from the dispenser needle in a semi-molten form. After being dispensed on the substrate layer-by-layer, the cold filaments combine into a solidified product.[14] Foster *et al.*[25] have recently proposed fused deposition molding (FDM) of graphene-based polylactic acid filaments (GR-PLA) to fabricate disc-shaped anodes. These anodes,[25] similar to perforated GR-PLA substrates developed by Cohen *et al.* for 3D micro-batteries[11] circumvent the requirement for a current collector, thus offering a simplistic and cheaper alternative to traditional Li-ion based setups.[11,25] The GR-PLA electrodes when tested *vs.* Li delivered very low capacity varying from 0.6 to 15.8 mA h g^{-1}.

Our current research is a feasibility study of the fabrication of electrochemically active $Li_4Ti_5O_{12}$ (LTO)-based anode and $LiFePO_4$ (LFP)-based cathode filaments. To the best of our knowledge, the FFF method for LTO- and LFP-based Li-ion battery electrodes has not been covered in the literature, to date. This is the first step toward a smart 3D Printable Micro-battery (3DPM), in which all the battery components – the anode and cathode current collectors, the anode layer, the cathode layer and the ion-conducting membrane or solid electrolyte are fabricated concurrently, thus enabling free form-factor batteries. We address, in addition, the possibility of the fabrication of the different cross-section, electrode networks (EN) in a specific arrangement, which deals with the continuous volumetric changes in the electrodes occurring during charge/discharge and operates as a multi-metamaterial system.

Results and discussion

The FFF method opens the possibility of miniaturization and free form-factor battery design, fewer dead-mass components,

lower energy losses, and provides well-defined interfaces and better energy-transfer efficiency. We propose the free form-factor 3DPM designs, which imply forming thin interlaced fiber-like electrode networks. The ENs may be rectangular, cubical, prismatic, spherical, or may have any other desirable, tailored-to-application shape. Some examples of ENs are shown schematically in Fig. 1A. These, similar to the fiber scaffolds proposed for bone-tissue engineering, can be of regular or irregular structures.[26]

The anode and cathode incorporate respective current collector networks, thus forming a core/shell current collector/electrode structure. The cross-sectional shape of the anode and cathode core–shell structures can be hexagonal, cubic, circular and spiral. The cross-sectional thickness of the "shell" anode and/or the "shell" cathode in the center of the electrode may vary from the thickness at the perimeter possessing gradient anisotropy (Fig. 1B). Fig. 1C is a schematic, pictorial illustration of the internal view of a 3D printed battery. It is obvious that the thinner the current collector, the higher the interfacial area between it and the electrode material, followed by higher power capability of the battery. In the 3D-EN battery, the free space between the interlaced cathode and anode nets is "filled" with solid electrolyte or quasi-solid electrolyte.

To evaluate the area gain of simplified interlaced electrode network architectures the following calculations have been carried out. We assume that ENs are made of two rectangular
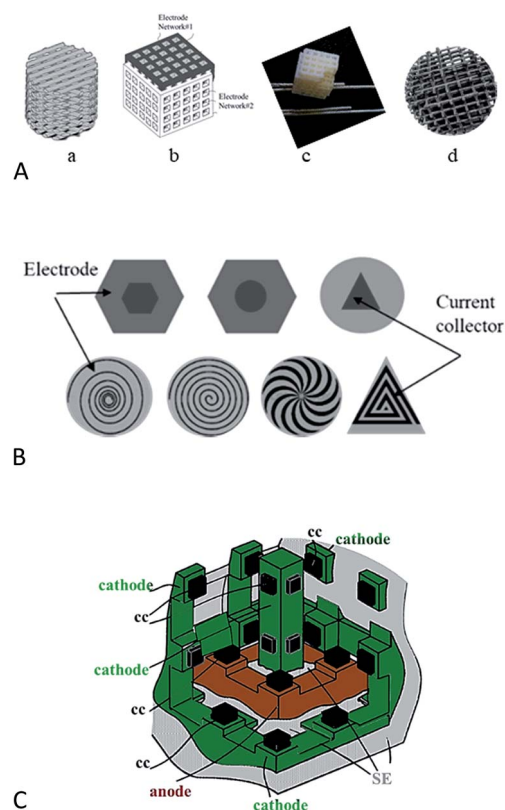

Fig. 1 (A) Schematics (a and b) and 3D printed models (c and d) of the interlaced electrodes networks. (B) Schematics of the cross sectional views of core–shell electrodes. (C) Pictorial view of a 3D battery.

interlaced 3D arrays of fiber-like electrodes. The fibers have a rectangular cross-section measuring $D \times D$. The distance between the fibers is d. There are N fibers in a row, where N is the number of fibers that can be introduced along a line parallel to the side of the cube with length L:

$$N = \text{floor}(L/d)$$

Floor (X) denotes that if the ratio L/d is not an integer, one uses the lowest closest integer bounding X. The array has fibers in three orthogonal Cartesian directions along the sides of the cube. The surface area of the arrays is $A_{S3} = 12N^2D(L - ND)$. Note that the area of an array that has fibers only in one direction is $A_{S1} = 4N^2DL$. Thus, the area gained using a 3D array has a ratio of:

$$A_{S3}/A_{S1} = 3 - 3ND/L \approx 3 - 3D/d$$

The thinner the fibers are and the smaller the distance between them is, the larger is the area gain of A_{S3} compared to A_{S1}. The area of a square 2D battery with a footprint of the cube is L^2. The area gained by the 3D array has a ratio of:

$$A_{S3}/A = 12N^2D(1/L - ND/L^2) \approx 12DL/d^2(1 - D/d)$$

Since $d > D$ and $L \gg d$ this ratio is positive and larger than 1. The volume of a 3D array is:

$$V_{S3} = L^3 + 2N^3R^3 - 3N^2LR^2$$

The volume between the interlacing 3D fiber arrays is:

$$V_e = L^3 - 2V_{S3} = 6N^2LD^2 - 4N^3D^3 - L^3 \approx L^3(6(D/d)^2 - 4(D/d)^3 - 1)$$

Examining the formula of the approximated volume we notice that the volume exists if and only if: $(1 + \sqrt{3})/2 \geq D/d \geq 0.5$. This limit bounds the distance D.

Fig. 2 illustrates the area and the area to volume ratio A_{S3}/V_{S3} of a cubic EN with a length of $L = 10$ mm. The range of D is between 0.1 and 0.5 mm and d is between $1.1D$ and $1.85D$. This

is different from the approximated boundaries of $[0.73D, 2D]$ we derived from the approximated volume because of the floor function.

V_{S3} increases steeply with d and increases slowly with D. The maximal volume is achieved at $D = 0.5$, and $d = 0.925$ and it is $V_e = 500$ mm^3. The surface area increases when D and d are small, and the maximal surface area is $A_{S3} = 17\,776$ mm^2. For example, if we use an array with $L = 10$ mm; $D = 0.1$ mm and $d = 0.183$ mm its surface area will be $A_{S3} = 16\,096$ mm^2 compared to a unidirectional array of $A_{S1} = 12\,178$ mm^2 or a 2D array of $A_{S1} = 100$ mm^2. The volume of active material (V_{S3}) is 440.12 mm^3, the volume between the arrays (V_e) is 119.74 mm^3, which provides an area to volume ratio of $A_{S3}/V_{S3} = 134.42$ mm^{-1}. As expected, the thinner are the electrode fibers, and the smaller is the distance between them, the higher is the surface area to volume ratio of the interlaced network structure. Metamaterials are considered a new class of artificial materials that derive their properties from newly designed structures and not from the composition and intrinsic properties of the material. An ideal mechanical metamaterial for printed electrochemical energy storage devices would simultaneously possess two or more of the following properties: high stiffness, high strength, high toughness, reversible stretchability, low mass density and electrochemical activity. In addition to the idea of concurrent fused-filament fabrication of all components of the battery, we assume that the placing of multi-material ENs (Fig. 1C) in a rationally designed arrangement will enable us to deal with the continuous volumetric changes in the electrodes occurring during charge/discharge. As a result, the battery is expected to function as a multi-metamaterial electrochemical system. From the perspective of a battery designer, it is important to know the limits of the mechanical flexibility of batteries for a given combination of the electrode architecture and current collectors, and to know the relationship between structural changes within the battery and the electrochemical performance of the battery. This, of course, requires comprehensive computing, which has recently begun in our group.

At present, nearly arbitrary, three-dimensional EN architectures from multiple classes of materials can be printed by the FFF method with minimum feature dimensions of 100 μm. Fig. 3a shows disc and spiral shaped LTO-PLA and LFP-PLA electrodes printed by the FFF method. The last optical image on the right is of particular interest since it represents the double-spiral multi-material sample, in which both spirals are simultaneously printed by the FFF method. The inner ring is the BLACKMAGIC3D current collector and the outer one is that of the LTO-PLA composite. The filaments used for the fabrication of electrodes were prepared by extrusion and contained 50–70% active material, 10% carbon additives and 20–40% PLA. The composite LFP-PLA and LTO-PLA homemade filaments have sufficient flexibility, ductility and toughness.

Fig. 3b and c show the ESEM micrographs of the initial and the succeeding steps of the FFF printing of spiral LiFePO$_4$-PLA and Li$_4$Ti$_5$O$_{12}$-PLA electrodes at different magnifications. Fig. 3d shows the printed double spiral structure of the BLACKMAGIC3D current collector and the morphology of the printed LTO-PLA anode. It is well established that the use of
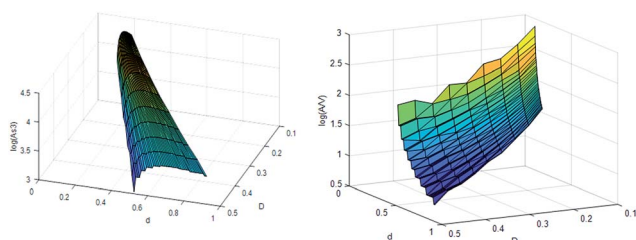

Fig. 2 Surface area (left) and area-to-volume ratio (right) of rectangular electrode networks.
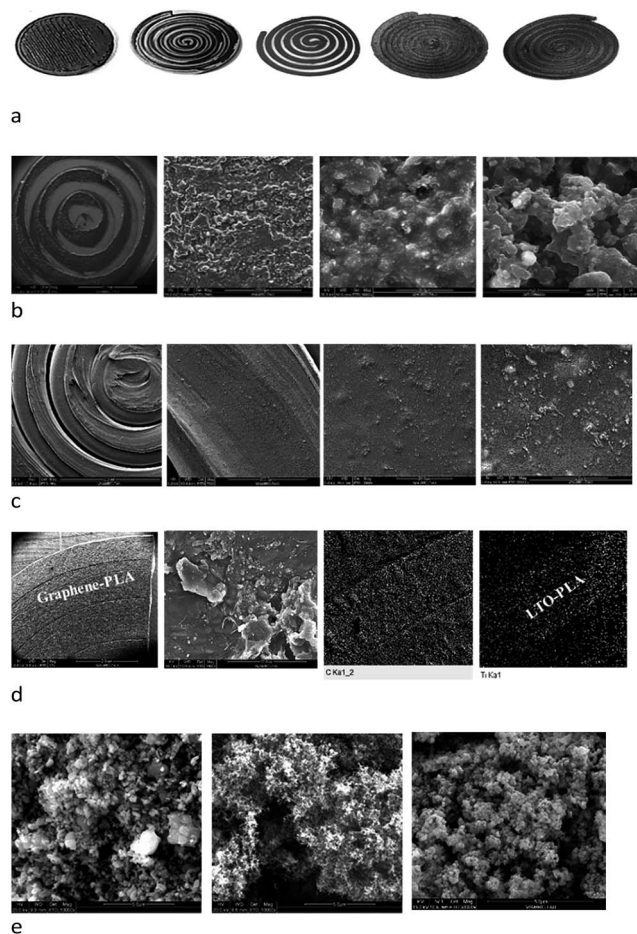
Fig. 3 (a) Optical images of printed electrodes (left to right) LFP-PLA, LTO-PLA, LFP-PLA, LTO-PLA/graphene-PLA. (b) ESEM images of LFP-PLA electrodes. (c) ESEM images of LTO-PLA electrodes. (d) ESEM and EDS mapping images of LTO-PLA/graphene-PLA double spiral. (e) ESEM images of (left to right): pristine LFP, C65 and LTO powders.

nanosize LFP and LTO particles (Fig. 3e) is advantageous as a result of the enhanced ionic diffusion of Li^+. However, in order to create continuous electron percolation in the electrode, supplementary carbon additives are necessary. This requirement, similar to that for commercial electrodes prepared by the doctor-blade casting method, is valid for the printed electrodes, as well. Close inspection of the high-magnification images of printed LFP-based cathodes (Fig. 3b) shows strong agglomeration of particles and the formation of a porous structure. The electrode surface displays significant roughness and complete coverage of the LFP particles by the PLA polymer. The surface morphology of the LTO-based anode is much smoother and denser (Fig. 3c). The individual LTO particles cannot be resolved in the ESEM micrographs, indicating that the intermixing of the anode components seems to be better than of the cathode composite. We attribute this to the higher surface charge and zeta-potential of lithium titanate in dioxolane solvent (used for the preparation of the initial slurry for the extruder), than those of lithium iron phosphate particles. The formation of the double-spiral LTO-PLA/graphene-PLA

structure by the FFF method is proved using ESEM micrographs and EDS mapping.

TOF-SIMS images of composite electrodes printed by the FFF method show the lateral distribution of components (Fig. 4) acquired in the positive-ion mode. The data support the ESEM tests. The most intensive mass peak of polymer species in the spectra is that with a nominal mass of 56, which corresponds to the $C_3H_4O^+$ ion which is formed by the bombardment of PLA. The intensity of the lithium-cation signal in the mass spectra was found to be higher than that of iron and so, Li^+ was used to image the spatial distribution of the LFP and LTO. As can be seen from the comparison of TOF-SIMS images, higher Li^+ ion yields and better homogeneity are observed for the LTO-based anode than for the LFP-based cathode. The images of the double-spiral LTO current-collector structure clearly show the signal of the lithium cation in the outer anode ring (image in the center) and its absence from the inner ring, which is related to the current collector. In this case, the overlay (the right image) combines two images of carbon and lithium species obtained in positive and negative ion modes. The carbon ion image (in negative ions) is obtained after Cs sputtering, and the high C^- intensity comes mainly from the carbon content in PLA of the anode, electron conducting additives and the graphene component of BLACKMAGIC3D. The lithium ion image (in positive ions) is obtained after oxygen sputtering and it highlights the PLA-LTO area of the double spiral.

The results of electrochemical testing of Li/LFP and Li/LTO microbatteries assembled in a coin-cell setup are shown in Fig. 5. It is important to emphasize that the profiles of voltage *vs.* the charge/discharge time and *vs.* state-of-charge of the cells
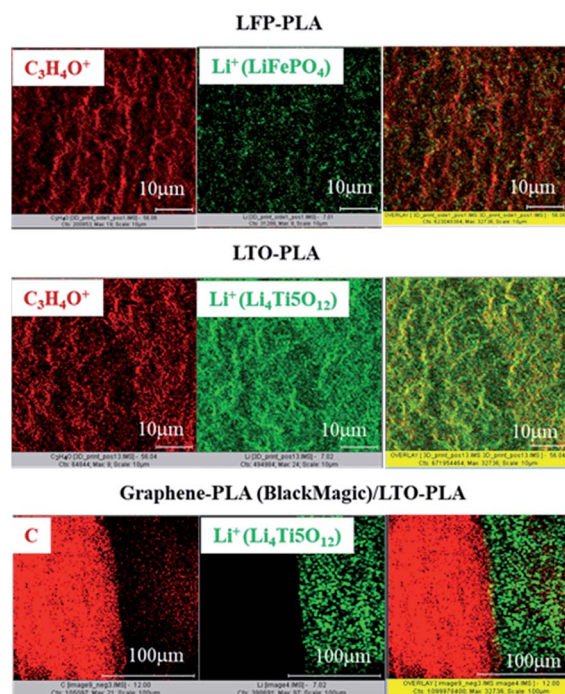

Fig. 4 TOF-SIMS images of printed LFP-PLA, LTO-PLA electrodes and double spiral comprising graphene-PLA (BlackMagic) and LTO-PLA parts.
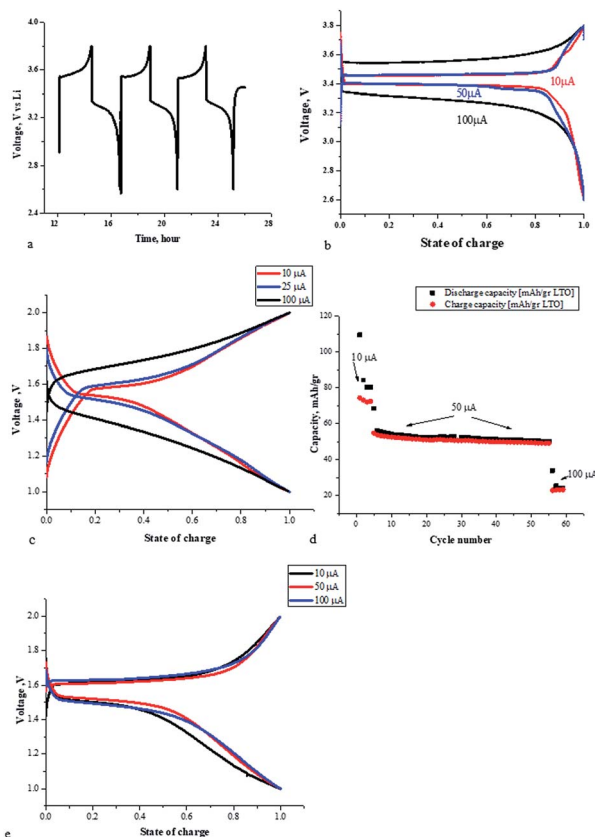
Fig. 5 Charge/discharge profiles (a–c and e) and cycle life (d) of Li/LiPF$_6$: EC:DEC/LFP (a and b), Li/LiPF$_6$: EC:DEC/LTO (c and d) and Li/0.3 M LiTFSI–PYR$_{14}$TFSI/LTO (e) cells at 50 °C.

containing printed LFP or LTO electrodes are similar to typical profiles of the cells with commercial electrodes. The voltage profile of the LFP-PLA cathode cycled between 3.8 and 2.6 V is presented as a function of capacity at 9 µA cm^{-2}, 44 µA cm^{-2} and 88 µA cm^{-2} charge- and discharge-current densities. The cycling of the cell resulted in 60, 50 and 20 mA h g^{-1} for LFP at 9, 44 and 88 µA cm^{-2}, respectively. The data show the utilization of about 50% of the theoretical capacity of the LFP cathode at a very low cycling rate. The utilization of the electrode-active material depends on the complex interplay between the electronic conduction created by carbon additives and the ionic conductivity of the composite-polymer electrode. Since PLA is not a lithium ion-conducting polymer, its ionic conductivity is obtained by the formation of a gel following the swelling of the polymer with liquid organic electrolytes or ionic liquids.[27] The limited utilization of the active material originates from the non-optimal distribution of active electrode materials and conducting additives and the long diffusion path of lithium ions in the polymer phase, caused by the combined effect of thick electrodes and insufficient amount of the impregnated electrolyte. Increase in current density on cycling of the Li/LFP cell by an order of magnitude is followed by a 3.5 times increase of the charge–discharge overpotential at 50% state-of-charge, while for the Li/LTO cell the overpotential growth is half of that. This may be caused by the poor homogeneity and higher

resistance of the printed LFP cathode. At low C-rates, the specific capacity of the Li/LTO cell is 80 mA h g^{-1}, which is also only 50% of the theoretical value for LTO. The Li/LTO cell runs for 60 reversible cycles at 30 µA cm^{-2} (Fig. 5d) and the test continues. The capacity increased by 10% when a double-spiral LTO current collector was used. The reversible capacity of Li/0.3 M LiTFSI–PYR$_{14}$TFSI/LTO cells is lower than that in the cell with a non-aqueous carbonate-based battery electrolyte. This indicates the commonly observed lower conductivity of ionic liquid electrolytes.[25] However, since the charge/discharge overpotential of the cell is only slightly influenced by the operation at different C-rates (Fig. 5e), we may suggest that the wettability of the printed LTO-PLA electrode by the ionic-liquid electrolyte is good. We believe that the data presented above are proof of the concept of successful printing of free form-factor battery electrodes by fused-filament fabrication.

The data presented here are the preliminary results of ongoing research. Further maximization of the utilization of the active material is currently being carried out by optimization of the content and tailoring the porosity and microstructure of the composite polymer electrode. This is done by changing the polymer type and conductive additive type; the polymer-to-active material and polymer-to-conducting additive ratio; and usage of volatile plasticizers, like low-molecular-weight poly-ethylene glycol or propylene carbonate. Our aim is to improve the percolation of the active material with the conducting additives, to enhance liquid-electrolyte impregnation into the composite-polymer electrodes to develop printable solid electrolyte and, finally, a solid-state free form-factor battery.

Experimental

For the initial experiments we chose polyester polylactic acid (PLA) (PLA L-175 Purac® Corbion), made from lactic acid monomer units. PLA is a thermoplastic polymer stable up to high temperatures, with a melting point of 170–180 °C and a degradation temperature of above 200 °C. PLA pellets were dissolved in 1,3-dioxolane (Sigma-Aldrich) under stirring for 12 hours at room temperature. Commercial LiFePO$_4$ (LFP) powder (Life Power P2, Clariant) as an active cathode material, graphite powder (SkySpring Nanomaterials, Inc), graphitized multi-walled (–COOH) – functionalized carbon nanotubes (US Research Nanomaterials, Inc) and C65 carbon (Timical) were dispersed in a ratio of 25 : 15 : 5 : 5% (w/w), respectively, with the use of a Thinky mixer ARE-250 (Thinky, Japan) at 1500 rpm for 15 minutes. The resulting homogeneous slurry was poured on a Teflon plate and dried for 12 hours at room temperature. After drying, it was crushed to the size of small composite pellets to be used for the fabrication of filaments. LFP/PLA/carbon composites were extruded with a Noztek Pro filament extruder (Noztek, London) to form a filament suitable for use as feedstock in a fused-deposition 3D printer. With appropriate choice of the nozzle diameter (in the range of 1.4–1.7 mm) and careful control of the nozzle temperature (typically in the range 190–210 °C) and the extrusion speed, filaments were produced with a circular cross section of average diameter 1.75 mm and a typical standard deviation of 0.02–0.03 mm. Lithium titanate

($Li_4Ti_5O_{12}$, LTO, Sud-Chemie Clariant) was used as an active material for the fabrication of anode filaments. The LTO-to-carbon and LTO-to-PLA ratios were the same as in the cathode.

A double-spiral current-collector/electrode network was printed with the use of the BLACKMAGIC3D filament (Graphene 3D Lab) and the LTO-PLA anode. The printing was done with a Up-Plus 2 printer by UP3D. Printed-disc and spiral-shaped electrodes with a diameter of 15 mm and a thickness of 200 μm were used as our first printed model cathode. The fabrication process of the anode was similar to that of the cathode. $Li_4Ti_5O_{12}$ (LTO) powder (Life Power C-T2, Sud-Chemie Clariant) was used as an active anode material.

The printed samples were dried under vacuum at 100 °C for 12 hours in order to remove residual solvent and moisture. For the initial 3DP-cathode and anode feasibility tests, 3D-printed batteries (3DPB) were fabricated in coin cells (type 2032). The 3DPB cells used in this work comprised a stainless-steel current collector, a Celgard separator soaked in commercial electrolyte (1 M $LiPF_6$ in 1 : 1 EC : DEC, 2% VC) or 0.3 M $LiTFSI$–$PYR_{14}TFSI$ ionic-liquid electrolyte, and a lithium-anode foil. The 3D-printed cathode and anode were vacuum impregnated with the electrolyte for 5 minutes prior to cell construction. All subsequent handling of these materials took place under an argon atmosphere in a MBraun glove box containing less than 1 ppm water and oxygen.

The 3DP electrochemical coin cells were constructed and electrochemically investigated by EIS, CV and galvanostatic cycling with a BCS-805 Biologic Instrument at 50 °C. The charge–discharge tests were carried out in current-control mode at various current densities.

Surface ESEM micrographs of the 3DPB samples were taken with a Quanta 200 FEG ESEM. The samples were sputtered with a thin gold film (6 nm) prior to the scanning. TOF-SIMS tests were performed with the use of a TRIFT II (Physical Electronics Inc., USA) under the following operating conditions: primary ions In^+, DC-sputtering rate 0.035 nm min^{-1} based on SiO_2 reference.

Conclusions

Our research efforts have culminated in the development of unique designs of 3D microbatteries. The disc, spiral and double-spiral shaped composite LFP-PLA cathode and LTO-PLA anode have been printed by the fused-filament fabrication method. The morphology of the printed LTO anode was found to be smoother and the lateral distribution of LTO and the polymer is more homogeneous than that of LFP and PLA. The proof of concept of the FFF-printed battery was demonstrated by the electrochemical activity of the electrodes in the cells vs. the lithium metal anode. Although our experiments showed partial utilization of about 50% of the theoretical capacity of the LFP cathode and 60% of the double-spiral current collector/LTO anode, we are confident that these findings will pave the way for a complete FFF printing of microbatteries. To achieve high performance of batteries and full utilization of the active material in the printed electrodes, the composition and morphology of electrodes, compatibility and miscibility of

components, and the parameters of the FFF printing technique should be optimized. We propose new architectures of different cross-section electrode networks, which will deal with continuous charge/discharge volumetric changes and operate as a multi-metamaterial system. Taking into account that PLA is a bio gradable polymer, the ability of FFF battery technology to interact with nature without a permanent negative influence is highly desirable.

The proposed concept is not exclusive for batteries at the microscale, but gives rise to a multi-disciplinary range of applications from macro 3D free form-factor batteries for vehicles to implantable nano-energy storage devices and energy harvesting components.

Conflicts of interest

There are no conflicts to declare.

Acknowledgements

References

1 M. Roberts, P. Johns, J. Owen, D. Brandell, K. Edstrom, G. El Enany, C. Guery, D. Golodnitsky, M. Lacey, C. Lecoeur, H. Mazor, E. Peled, E. Perre, M. M. Shaijumon, P. Simon and P.-L. Taberna, *J. Mater. Chem.*, 2011, **21**, 9876.
2 C. Wang, L. Taherabadi, G. Jia, M. Madou, Y. Yeh and B. Dunn, *Electrochem. Solid-State Lett.*, 2004, **7**, A435.
3 M. Nathan, D. Golodnitsky, V. Yufit, E. Strauss, T. Ripenbein, I. Shechtman, S. Menkin and E. Peled, *J. Microelectromech. Syst.*, 2005, **14**(5), 879–885.
4 B. Sun, H. D. Asfaw, D. Rehnlund, J. Mindemark, L. Nyholm, K. Edstrom and D. Brandell, *ACS Appl. Mater. Interfaces*, 2017, **10**(3), 2407–2413.
5 H. Mazor, D. Golodnitsky, L. Burstein, A. Gladkich and E. Peled, *J. Power Sources*, 2012, **198**, 264–272.
6 S. Ferrari, M. Loveridge, S. D. Beattie, M. Jahn, R. J. Dashwood and R. Bhagat, *J. Power Sources*, 2015, **286**, 25–46.
7 J. F. M. Oudenhoven, L. Baggetto and P. H. L. Notten, *Adv. Energy Mater.*, 2011, **1**, 10–33.
8 J. Xie, J. F. M. Oudenhoven, D. Li, C. Chen, R.-A. Eichel and P. H. L. Notten, *J. Electrochem. Soc.*, 2016, **163**, A2385–A2389.
9 K. Dokko, J. Ichi Sugaya, H. Nakano, T. Yasukawa, T. Matsue and K. Kanamura, *Electrochem. Commun.*, 2007, **9**, 857–862.
10 T. S. Arthur, D. J. Bates, N. Cirigliano, D. C. Johnson, P. Malati, J. M. Mosby, E. Perre, M. T. Rawls, A. L. Prieto and B. Dunn, *MRS Bull.*, 2011, **36**, 523–531.
11 E. Cohen, S. Menkin, M. Lifshits, Y. Kamir, A. Gladkich, G. Kosa and D. Golodnitsky, *Electrochim. Acta*, 2018, **265**, 690–701.
12 X. Tian, J. Jin, S. Yuan, C. K. Chua, S. B. Tor and K. Zhou, *Adv. Energy Mater.*, 2017, **7**, 1–17.

13 C. Zhu, T. Liu, F. Qian, W. Chen, S. Chandrasekaran, B. Yao, Y. Song, E. B. Duoss, J. D. Kuntz, C. M. Spadaccini, M. A. Worsley and Y. Li, *Nano Today*, 2017, **15**, 107–120.

14 C. Du, Q. Liang, Y. Luo, Y. Zheng and Q. Yan, *J. Mater. Chem. A*, 2017, **5**, 22442–22458.

15 D. Golodnitsky, E. Strauss and S. Menkin, in *Printed Batteries: Materials, Technologies and Applications*, ed. C. M. C. Senentxu Lanceros-Méndez, John Wiley & Sons, Inc, 1st edn, 2018.

16 F. Zhang, M. Wei, V. V. Viswanathan, B. Swart, Y. Shao, G. Wu and C. Zhou, *Nano Energy*, 2017, **40**, 418–431.

17 E. Malone, K. Rasa, D. Cohen, T. Isaacson, H. Lashley and H. Lipson, *Rapid Prototyp. J.*, 2004, **10**, 58–69.

18 R. R. Kohlmeyer, A. J. Blake, J. O. Hardin, E. A. Carmona, J. Carpena-Núñez, B. Maruyama, J. Daniel Berrigan, H. Huang and M. F. Durstock, *J. Mater. Chem. A*, 2016, **4**, 16856–16864.

19 K. Sun, T. S. Wei, B. Y. Ahn, J. Y. Seo, S. J. Dillon and J. A. Lewis, *Adv. Mater.*, 2013, **25**, 4539–4543.

20 K. Fu, Y. Wang, C. Yan, Y. Yao, Y. Chen, J. Dai, S. Lacey, Y. Wang, J. Wan, T. Li, Z. Wang, Y. Xu and L. Hu, *Adv. Mater.*, 2016, **28**, 2587–2594.

21 Y. Hu and X. Sun, *J. Mater. Chem. A*, 2014, **2**, 10712–10738.

22 J. Hu, Y. Jiang, S. Cui, Y. Duan, T. Liu, H. Guo, L. Lin, Y. Lin, J. Zheng, K. Amine and F. Pan, *Adv. Energy Mater.*, 2016, **6**, 1–8.

23 D. Zhang, B. Chi, B. Li, Z. Gao, Y. Du, J. Guo and J. Wei, *Synth. Met.*, 2016, **217**, 79–86.

24 J. Li, M. C. Leu, R. Panat and J. Park, *Mater. Des.*, 2017, **119**, 417–424.

25 C. W. Foster, M. P. Down, Y. Zhang, X. Ji, S. J. Rowley-Neale, G. C. Smith, P. J. Kelly and C. E. Banks, *Sci. Rep.*, 2017, **7**, 42233.

26 S. Gómez, M. D. Vlad, J. López and E. Fernández, *Acta Biomater.*, 2016, **42**, 341–350.

27 I. Osada, S. M. Hosseini, S. Jeong and S. Passerini, *ChemElectroChem*, 2017, **4**, 463–467.